High-Speed Tomographic PIV in an IC Engine

Marco Braun[1,*], Wolfgang Schröder[1], Michael Klaas[1]
1: Chair of Fluid Mechanics and Institute of Aerodynamics, RWTH Aachen University, Aachen, Germany
* Correspondent author: m.braun@aia.rwth-aachen.de

Keywords: PIV, combustion engine, tomography, high-speed, HS-TPIV

ABSTRACT

Novel combustion engine processes like Controlled Auto Ignition (CAI) and Homogeneous Charge Compression Ignition (HCCI) aim at an instantaneous ignition of a homogenous fuel-air mixture formation to reduce pollutant emissions, i.e., soot formation and NO_x generation, and to improve engine efficiency. However, the in-cylinder flow field is characterized by the development of time-dependent and highly three-dimensional large-scale flow structures and cycle-to-cycle variations (CCV). To investigate these large-scale flow structures and the CCV inside the combustion chamber at high temporal resolution, high-speed volumetric velocity measurements are required.

In this study, a high-speed tomographic particle-image velocimetry (HS-TPIV) setup is used to measure the velocity field in an internal combustion engine (ICE) at an engine speed of 1,500 rpm and at a temporal resolution of 10° crank angle (CA) in a maximum measurement volume of 50x8x83 mm³. The HS-TPIV results are validated using high-speed stereoscopic particle-image velocimetry (HS-SPIV) measurements in the engine's tumble plane. The tumble plane is extracted from the volumetric data of the HS-TPIV results for the comparison to the HS-SPIV measurements. The measurements show that HS-TPIV yields reliable measurements of the 3D flow field, although slight differences to the HS-SPIV can be observed.

The comparison of the ensemble-averaged volumetric flow fields for three different intake pressures, namely 1.0 bar, 1.2 bar, and 1.4 bar, shows that the intake pressure has an impact on the flow field topology. While the velocity distribution inside the engine slightly changes when the intake pressure is increased, the volume-averaged velocity level remains almost the same since higher intake pressure increases the velocity in some regions of the combustion chamber, while the velocity in other regions is decreased. The results show that the size of the core of the tumble vortex slightly increases towards top dead center and that its trajectory through the cylinder is more well-rounded for higher boost pressure.

1. Introduction

One of the major challenges that society is facing today is the increasing energy demand of the worldwide transportation sector. This rising fuel demand will lead to a significant decrease in the availability of fossil energy carriers, and the depletion of the worldwide oil reserve was anticipated to 2043 by different authors (Shafiee and Topal, 2009; Singh and Singh, 2012). Moreover, legislation

aims at drastically reduced pollutant emissions to counteract the global increase in air pollution and greenhouse gas emissions.

On the one hand, the development of fuels from renewable feedstock can help to compensate the declining resources of oil and gas. On the other hand, modern biofuels often show improved combustion processes with reduced emissions (Hoppe et al., 2016; Thewes et al., 2011; Brassat et al., 2011) and their high amount of molecular bonded oxygen can lead to a significant reduction of NO_x emissions (Janssen et al., 2009). Additionally, biofuels enable more freedom concerning mixture formation (Braun et al., 2017) and ignition timings (Hoppe et al., 2016; Daniel et al., 2011). In addition, novel engine technologies have been developed over the last couple of years and are still being further developed to reduce the amount of pollutant emissions, to improve fuel efficiency, and to spare fuel resources. Two novel combustion concepts are Controlled Auto Ignition (CAI) and Homogeneous Charge Compression Ignition (HCCI). These concepts are based on the instantaneous ignition of a homogenous fuel-air mixture using the temperature increase of the compression instead of a spark plug to initiate the ignition. The homogeneous combustion reduces soot formation and the peak combustion temperature, which is the main factor for NO_x generation. Additionally, HCCI makes throttling obsolete during partial load and, hence, further increases engine efficiency (Baumgarten, 2006).

These combustion concepts require a homogeneous mixture of air and fuel, which is generated by the mixing process during the intake and the compression stroke of modern internal combustion engines (ICE) (Druault et al., 2005; Heywood, 1988; Lumley, 1967). Hence, the flow field that develops during these two strokes has a direct influence on engine efficiency, fuel consumption, and pollutant emissions. The majority of studies that analyzed the engine flow field and the mixture formation during the intake and compression stroke focused on planar measurements and ensemble-averaged flow field quantities. However, the in-cylinder flow that is related to the mixture formation is characterized by highly three-dimensional and unsteady flow structures. Moreover, these structures are affected by cycle-to-cycle variations (CCV), which are defined as cycle dependent changes of the large-scale coherent flow structures. Thus, since the temporal and spatial development of the coherent flow structures and the CCV essentially affect the energy efficiency and emission output of ICE (Heywood, 1988; Lumley, 1999), volumetric and time-resolved measurements with high spatial resolution are an indispensable prerequisite for a detailed analysis of the in-cylinder flow field. However, three-dimensional measurements of the in-cylinder flow field inside combustion engines are still very rare in literature. The majority of tomographic particle-image velocimetry (TPIV) measurements in engines are conducted at low speed, e.g., van Overbrüggen et al. (2015) and Baum et al. (2012). These measurements provide a

detailed insight into the global features of the flow field during the intake and the compression stroke, e.g., the size and path of the tumble vortex, but do not possess the temporal resolution for an analysis of the CCV. Only very few research groups perform high-speed tomographic particle-image velocimetry (HS-TPIV) measurements (Singh et al., 2015; Gadekar et al., 2016) in IC engines, focusing on selected sub-regions of the in-cylinder flow field like the region beneath the inlet valves. Thus, the scope of this study is to measure the three-dimensional and time-dependent flow field in the combustion chamber of an optical single-cylinder ICE with a spatial and temporal resolution that, in general, allows for the analysis of both the large-scale flow structures and the CCV in large representative measurement volumes in the cylinder. The validity of the HS-TPIV measurements is validated using high-speed stereoscopic particle-image velocimetry (HS-SPIV) measurements of the engine's tumble plane. Following the validation, the influence of the intake pressure is investigated using the three-dimensional measurement results.

2. Experimental Setup and Methods

All PIV measurements of this study were conducted in a one-cylinder four-valve Otto engine with full optical access to the combustion chamber. The engine is a custom-made version (FEV GmbH, Aachen, Germany) of a direct-injection spark-ignition (DISI) ICE. It features a glass liner, two intake valves, two exhaust valves, a pent roof combustion chamber, and a flat piston crown. The engine's tumble port yields tumble numbers of approx. 2 – 4 depending on the crank angle (CA) (Bücker et al., 2012). The engine parameters are listed in table 1.

Tab. 1 Engine Parameters of the research engine TINA (btdc/atdc: before/after top dead center).

engine parameter	value
bore	75 mm
stroke	82.5 mm
displacement volume	364 cm^3
compression ratio	7.4:1
number of valves	4
valve lift	9 mm
intake valve diameter	27.1 mm
exhaust valve diameter	23 mm
intake valves open (1 mm lift)	12° atdc
intake valves close (1 mm lift)	196° atdc
exhaust valves open (1 mm lift)	204° btdc
exhaust valves close (1 mm lift)	20° btdc
connecting rod length	146 mm
crank radius	42.2 mm
oil temperature	∼ 60° C
intake temperature	∼ 20° C
intake pressure	1.0 bar; 1.2 bar; 1.4 bar
engine speed	1,500 rpm

To prevent the necessity of fuel combustion and to ensure full optical access to the combustion chamber, the engine is motored by a 30 kW electrical engine. For the application of optical measurements, the optical access to the combustion chamber is achieved by a quartz glass cylinder liner that covers the entire stroke. Furthermore, the engine's Bowditch design provides additional optical access to the combustion chamber from the bottom using a quartz glass piston crown and a 45°-mirror placed in the prolonged hollow piston. An oil conditioning system is used to preheat the engine oil to suitable operating conditions, to heat the engine, and to provide uniform operating conditions, while the engine's intake air conditioning system can be used to adjust the intake pressure.

For the HS-TPIV measurements, a Quantronix Darwin Duo 527-100-M (λ = 527 nm) high-speed laser with a maximum pulse energy of approx. 30 mJ was used to illuminate a measurement volume of 50x8x83 mm at a frequency of 900 Hz. The center section of the measurement volume was placed in the tumble plane and the pulse distance was set to 30 μs. The HS-TPIV setup is displayed in fig. 1 and the corresponding parameters are listed in tab. 2.

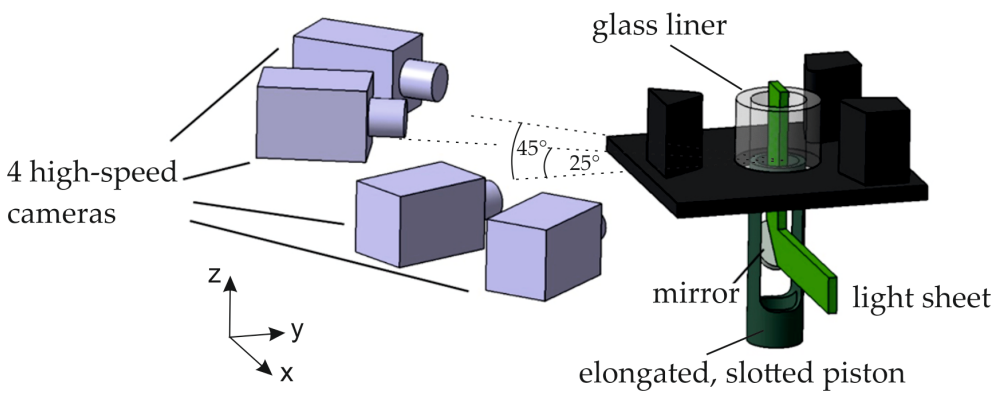

Fig. 1 HS-TPIV setup at the optical engine.

Tab. 2 Parameters of the high-speed tomographic particle-image velocimetry setup.

parameter	value
seeding particles	Di-Ethyl-Hexyl-Sebacat (DEHS)
mean particle diameter	$\sim$ 0.35 - 0.45 µm
laser	Darwin Duo 527-100-M
laser wavelength	527 nm (Nd:YLF)
laser frequency	900 Hz per cavity
laser pulse energy	$\sim$ 30 mJ/cavity (without losses)
laser pulse length	$\sim$ 210 ns per cavity
temporal resolution	10° CA
crank angle regime	50 - 330° atdc
measurement volume	$\sim$ 50x8x83 mm^3
pulse distance	30 µs
cameras	2x Photron Fastcam SA5, 2x Photron Fastcam SA3
viewing angle (SA3)	$\pm$ 25°
viewing angle (SA5)	$\pm$ 45°
lens	Tamron 180 mm macro
lens aperture	f/11
magnification	$\sim$ 0.2
sampled images	225 cycles @ 29 image pairs/cycle

The camera setup consisted of two Photron FASTCAM SA5 and two Photron FASTCAM SA3 high-speed cameras, which were equipped with Tamron 180 mm macro lens with a focal number of f/11 and Scheimpflug adapters to meet the Scheimpflug condition. The inner cameras (SA3) were set up with an angle of 25° in relation to the normal vector of the light sheet, while the outer cameras (SA5) utilized an angle of 45°.

The intake air was seeded with Di-Ethyl-Hexyl-Sebacat (DEHS) with a mean particle diameter of approx. 0.35 - 0.45 μm and the particle images were captured at a frequency of 1,800 Hz, which corresponds to 10° CA steps at an engine speed of 1,500 rpm. Following Bücker et al. (2013) and Benedict and Goud (1996), more than 200 engine cycles were recorded for each measurement for the calculation of the ensemble-averaged flow fields. The HS-TPIV measurements were conducted for three intake pressures, namely 1.0 bar, 1.2 bar, and 1.4 bar, to investigate the influence of the boost pressure on the engine flow.

The processing of the images was conducted using DaVis 8.4.0 by LaVision. For the calibration, five co-planar, equidistant calibration planes were recorded using a transparent single-plane calibration target with 176 circular markers. The calibration planes were located between y = -4 mm and y = 4 mm in steps of 2 mm. DaVis' calibration algorithm applied a 3rd order polynomial to calculate the transformation matrix using the calibration planes of all four views.

The raw images were separated by their crank angle position and the processing was conducted for each crank angle individually using all consecutive engine cycles. For every crank angle, a

sliding time filter was applied to subtract the minimum of a series of images to remove reflections and background illumination. Masks were applied for all four views to further remove reflections and to remove the irrelevant areas of the raw images. Thereafter, a 5x5 sliding minimum was subtracted to reduce background intensities due to multiple scattered light, and the image intensities were smoothed and normalized to the first image. A 3x3 Gaussian smoothing algorithm was applied to improve the image quality further.

The pre-processed images were used in several volume self-calibrations to further improve the quality of the transformation matrix and to reduce the deviation of the disparity to less than 0.48 pixels. Thereafter, DaVis' fast-MART algorithm was used to preform the volumetric reconstruction using 7 iterations with smoothing steps after each iteration step. The algorithm reconstructed the measurement volume of 50x8x83 mm^3 to 601x997x97 $voxels^3$, which calculates to approx. 0.083 mm/vox. Finally, the volume correlation was performed using a direct multi-pass correlation approach featuring 5 correlation windows steps with an initial windows size of 80x80x80 $voxel^3$ and a final window size of 32x32x32 $voxel^3$. The final vector field was calculated with 75 % vector overlap, which corresponds to a vector spacing of 8 voxels (0.67 mm). Between all correlation steps, three 5x5x5 universal outlier detection algorithms steps and five 3x3x3 smoothing steps were applied. After the final step, no smoothing was used.

Additional HS-SPIV measurements were conducted to validate the HS-TPIV measurements. For the stereoscopic measurements, only the two outer cameras were used and the light sheet was formed into a thin plane of approx. 1 mm to illuminate the tumble plane. Due to the reduced thickness of the measurement plane, the pulse distance was set to 20 μs to better capture the out-of-plane component of the velocity. Additionally, a focal number of f/8 was applied. The HS-SPIV measurements were processed with PIVView (PIVTEC GmbH, Germany) using a multi-grid algorithm with a final interrogation windows size of 32x32 pixel and 75% overlap. The processing of HS-SPIV measurements is described in detail in Braun et al. (2018). The validation of the quality of the HS-TPIV measurements was conducted for an inlet pressure of 1.0 bar, because the setup is identical for the other two test cases.

3. Flow Field Post-Processing

Since the flow field analysis focusses on the investigation of ensemble-averaged quantities, a Reynolds velocity decomposition is conducted for every measured crank angle position to separate the velocity $\vec{v}$ into an ensemble-averaged velocity $\bar{\vec{v}}$ and a velocity fluctuation $\vec{v}'$. For the x-direction, the ensemble-averaged velocity component calculates to

$$\overline{u\,(\Theta)} = \frac{1}{N}\sum_{n=1}^{N} u(\Theta, n) \quad ,$$

where N denotes the number of measured engine cycles and Θ denotes the crank angle. It should be noted that the fluctuation velocities acquired by the Reynolds decomposition contain both the turbulent fluctuations and CCV. A separation of the two is not conducted in this study, because the velocity fluctuation calculated from the Reynolds decomposition is widely used in literature and also a good qualitative measure of the turbulence. For the discussion of the energy fluctuations in the flow field over the progression of the crank angle, the kinetic energy is introduced as

$$e = \frac{1}{2}\left(\bar{u}^2 + \bar{v}^2 + \bar{w}^2\right) \quad ,$$

and the turbulent kinetic energy is calculated to

$$k' = \frac{1}{2}\left(u'^2 + v'^2 + w'^2\right) \quad ,$$

For the validation of the HS-TPIV measurements, the tumble plane is extracted from the volumetric HS-TPIV results. Thereafter, the extracted plane is evaluated using the planar calculation of flow field quantities, like it is conducted for the HS-SPIV results. With (i, j) as the coordinates of the cells in a two-dimensional field of a flow quantity f, the plane-averaged flow field quantity F is introduced as

$$F = \frac{1}{IJ}\sum_{i=1}^{I}\sum_{j=1}^{J} f_{i,j} \quad .$$

Thus, in the following, the plane-averaged kinetic energy is denoted as E and the plane- and ensemble-averaged turbulent kinetic energy is denoted as K. Furthermore, for the identification of the core of the tumble vortex, the Γ_1-criterion by Graftieaux et al. (2001) is calculated for each point (i, j) of the vector field using

$$\Gamma_1(i,j) = \frac{1}{S}\sum_{s=1}^{S} \frac{\vec{r} \times \vec{v}}{\|\vec{r}\| \cdot \|\vec{v}\|} \quad ,$$

where $\vec{r}$ is the position vector of a neighboring cell and $\vec{v}$ is the velocity vector of that cell. The parameter S denotes the number of neighboring cells used for the calculation of Γ_1. Following Dannemann et al. (2011), a 3x3 grid was chosen.

4. Results

In the following, the results of the HS-TPIV measurements are discussed. First, the results of the HS-TPIV measurements at 1 bar intake pressure are validated against the HS-SPIV measurements and the development of the flow field over an engine cycle is discussed. Afterwards, the three-

dimensional flow field results are discussed and the influence of an increasing intake pressure on the flow field is analyzed.

4.1 Validation of the HS-TPIV Measurements

To conduct the validation of the measurement results, the flow fields determined using the HS-TPIV setup are compared to the corresponding HS-SPIV results for selected crank angles, and the temporal development of the plane-averaged kinetic energy E and the plane- and ensemble-averaged turbulent kinetic energy K is compared.

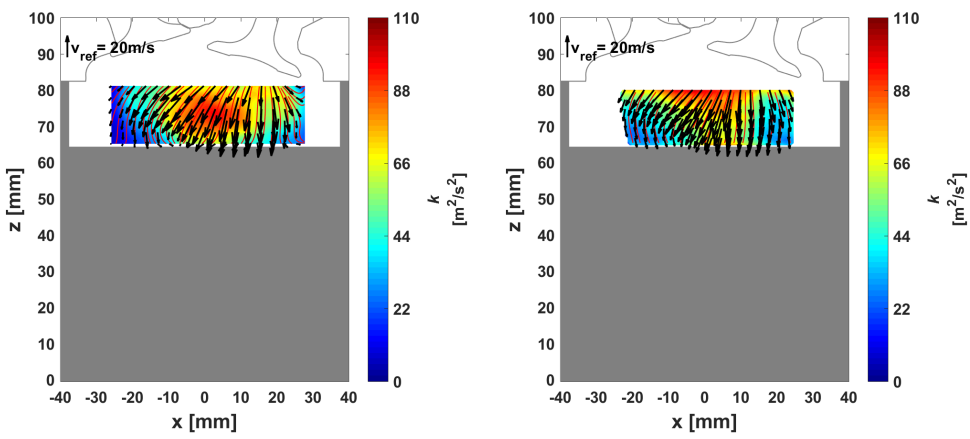

Fig. 2 Ensemble-averaged flow fields of the HS-SPIV (left) and HS-TPIV (right) results at 50° atdc. The plots show the ensemble-averaged turbulent kinetic energy k (color map), the ensemble-averaged velocity vectors (arrows), and streamlines (red lines) for 1,500 rpm in the tumble plane.

Figures 2 - 5 show the comparison of the flow fields for the HS-SPIV and the HS-TPIV measurements for four different crank angles. The plots display the ensemble-averaged turbulent kinetic energy k (color map), the ensemble-averaged velocity vectors (arrows), and the streamlines (red lines) for 1,500 rpm in the tumble plane. For the HS-TPIV results, the tumble plane was extracted from the volumetric data.

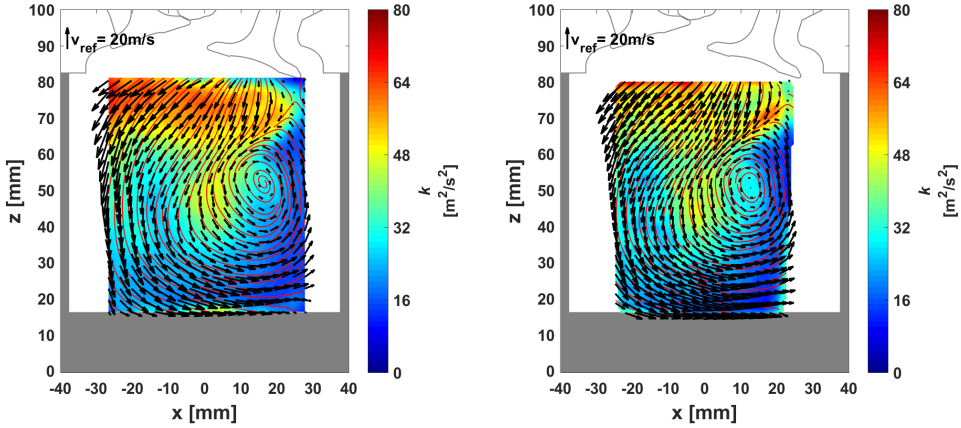

Fig. 3 Ensemble-averaged flow fields of the HS-SPIV (left) and HS-TPIV (right) results at 120° atdc. The plots show the ensemble-averaged turbulent kinetic energy *k* (color map), the ensemble-averaged velocity vectors (arrows), and streamlines (red lines) for 1,500 rpm in the tumble plane.

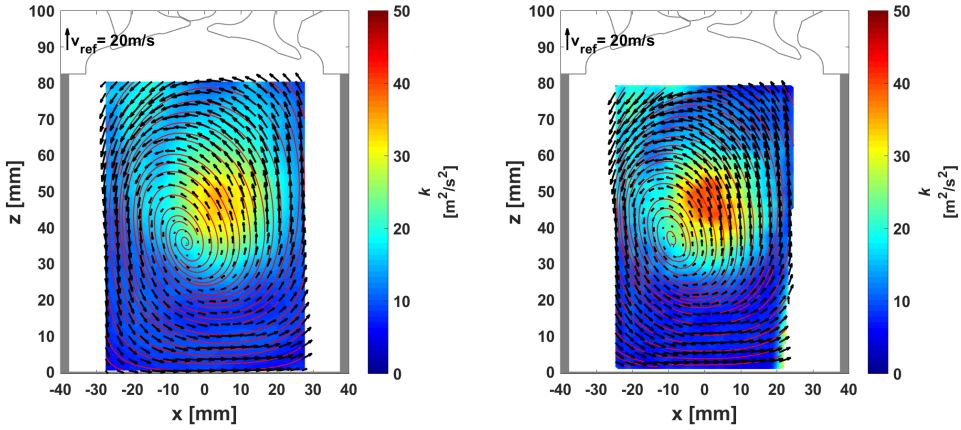

Fig. 4 Ensemble-averaged flow fields of the HS-SPIV (left) and HS-TPIV (right) results at 180° atdc. The plots show the ensemble-averaged turbulent kinetic energy *k* (color map), the ensemble-averaged velocity vectors (arrows), and streamlines (red lines) for 1,500 rpm in the tumble plane.

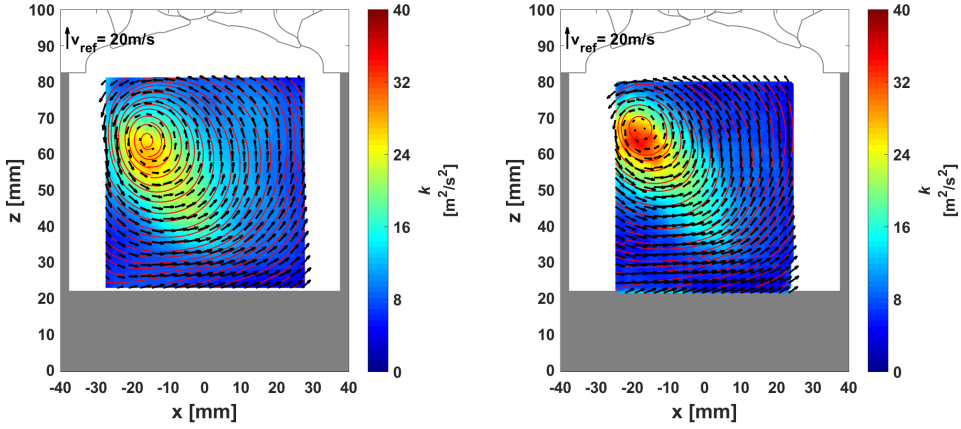

Fig. 5 Ensemble-averaged flow fields of the HS-SPIV (left) and HS-TPIV (right) results at 250° atdc. The plots show the ensemble-averaged turbulent kinetic energy k (color map), the ensemble-averaged velocity vectors (arrows), and streamlines (red lines) for 1,500 rpm in the tumble plane.

In figure 2, i.e., at 50° atdc, both measurements capture the high velocity of the intake jets, including the high turbulent fluctuations. However, some small differences can be observed. In the HS-TPIV results, the turbulent fluctuations are higher near the top of the measurement plane, which could be caused by some reflections or reduced seeding densities in some of the images. Note that differences at the far left and far right side of the vector fields are due to the different widths of the measurement planes in both measurements. Considering this, the velocities at the sides of the HS-TPIV result match the HS-SPIV results quite well.

Figure 3 displays the flow fields at 120° atdc. Here, the piston is gradually slowing down as it is moving towards the bottom of the combustion chamber after it had its maximum velocity at approx. 90° atdc. At this crank angle, the flow field features a well-developed, strong tumble vortex on the right side ($x > 0$) of the combustion chamber and declining turbulent fluctuations in the measurement plane due to the closing inlet valves and, hence, a decreasing velocity of the intake jets. Again, the flow topologies are very similar in both plots as the tumble vortex core is located at the same position in both images and the direction and magnitude of the velocity vectors are comparable. However, the turbulent kinetic energy in the upper center of the combustion chamber is slightly different, which is most probably due to fluid mechanical or experimental reasons, e.g., slight deviations in the boundary conditions or differences in the calibration procedure or in the processing.

At 180° atdc (fig. 4), the piston has reached the bottom dead center and the combustion chamber is at its maximum expansion. The valves are nearly closed at a valve lift of approx. 3 mm. Evidently, the velocity of the intake jets is mostly negligible and the flow field is dominated by the rotation of the tumble vortex, which now moves towards the opposite side of the combustion chamber. The comparison of both measurement techniques yields that the peak of the turbulent kinetic energy is slightly higher in the HS-TPIV results. However, in the HS-SPIV results, the turbulent kinetic energy possesses a slightly higher overall level in the combustion chamber, which eventually leads to similar energy levels over the entire plane for both cases.

During the compression stroke, the expansion of the combustion chamber is reduced again and the tumble vortex is directed towards the top dead center. Figure 5 displays the flow field at 250° atdc, where the tumble vortex is located in the top left corner of the measurement plane. Like at 180° atdc, the levels of the turbulent kinetic energy do not exactly match between both

measurements, since the turbulent kinetic energy has a higher peak in the HS-TPIV results and a slightly higher overall level in the HS-SPIV results.

For further validation, figure 6 shows the temporal progress of the plane-averaged kinetic energy E and the plane- and ensemble-averaged turbulent kinetic energy K over the crank angle. The kinetic energy in the measurement plane starts off very high at a crank angle of 50° atdc, since the small measurement volume is dominated by the high-velocity intake jets. Subsequently, the plane-

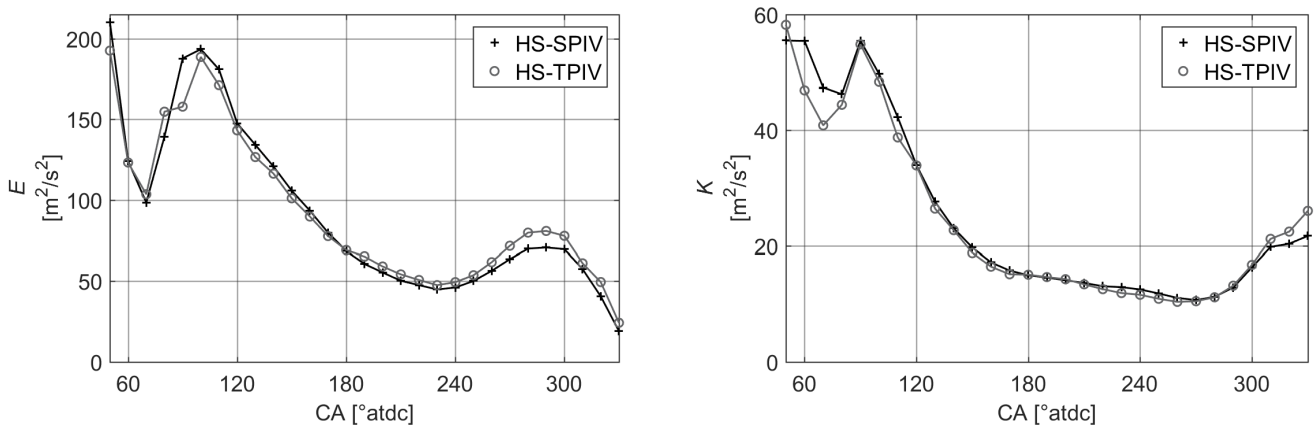

Fig. 6 Temporal progress of the plane-averaged kinetic energy E (left) and temporal progress of the plane- and ensemble-averaged turbulent kinetic energy K (right) over CA.

averaged kinetic energy decreases due to the downward moving piston, which also increases the size of the measurement plane. Afterwards, i.e., at approx. 70° atdc, the kinetic energy rises again, because the velocity of the intake jets and the velocities in the entire the flow field increase with increasing piston speed and valve lift. A similar behavior can be seen in the turbulent kinetic energy that mainly depends on the turbulent fluctuations due to the intake jets, which feature a very high velocity in the small valve gaps and shear layers between the intake jets and the rotating flow field of the tumble vortex. This can be also observed quite well in fig. 3. At approx. 90 - 100° atdc, the kinetic and the turbulent kinetic energy reach their maxima, followed by a decrease that ends at approx. 230° atdc. Here, halfway into the compression stroke, the so-called tumble spin-up begins and the tumble vortex starts to increase the kinetic energy inside the flow field since it moves towards the pent roof of the combustion chamber. At approx. 290° atdc, the tumble break-up leads to the decomposition of the tumble vortex in turbulent small-scale flow structures and the turbulent kinetic energy increases, while the kinetic energy decreases. Although the plots for both measurement techniques are in good agreement, small differences can be observed. The HS-TPIV results show slightly higher values towards top dead center. During the early intake stroke, the HS-TPIV results show a smaller turbulent kinetic energy (~ 5 m²/s²). Furthermore, at 90° atdc,

the HS-TPIV yields a dent in the progress of the kinetic energy that is probably a result of an over-prediction of the kinetic energy at 80° atdc.

Figure 7 illustrates the ensemble-averaged trajectory of the core of the tumble vortex in the tumble plane for both measurements. As mentioned above, the location of the vortex core is determined using the Γ_1-criterion. In both cases, the tumble vortex evolves in the top half of the combustion chamber slightly on the left side at approx. 70° atdc. Thereafter, the tumble vortex moves in negative z-direction and towards the right side of the cylinder. The vortex' furthest position in positive x-direction is reached at approx. 140° atdc with $x_{tumble} \approx 18\ mm$. Subsequently, the vortex core moves in a curve towards the opposite side of the combustion chamber. After the tumble reaches the bottom left corner of the measurement plane at 190° atdc, it is redirected towards the top left within only 20-30° CA and stays there for about 60° CA. Finally, the tumble moves back towards the center and leaves the measurement plane at approx. 320° atdc, because it is pushed into the engine's pent roof.

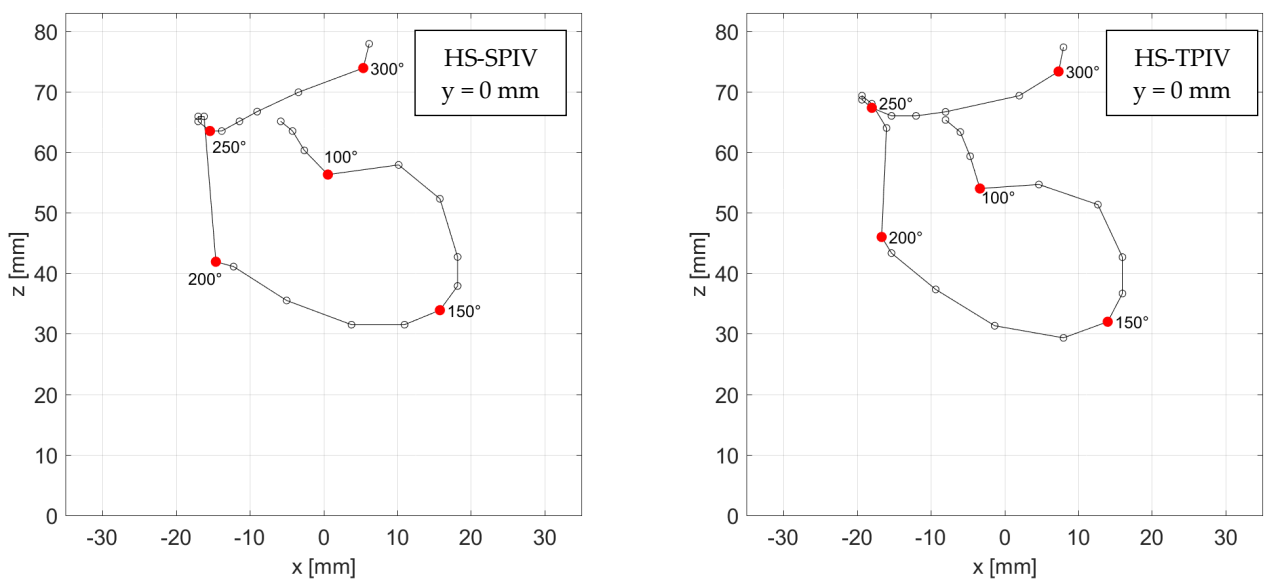

Fig. 7 Ensemble-averaged trajectory of the tumble vortex core in the combustion chamber in the tumble plane (y =0 mm) of the HS-SPIV (left) and HS-TPIV(right) for 1,500 rpm. The circles denote the location of the tumble vortex core between 70° atdc and 310° atdc in steps of 10° CA, while red dots display every 50° CA.

The comparison of both measurements shows a very good agreement of the path of the vortex core center. The maximum deviation can be found at 110° atdc and amounts to approx. 7 mm. All other deviations are significantly below that value. Again, small deviations in the ambient conditions or differences in the calibration and processing procedures are possible reasons for the deviations. Overall, it can be noted that the general flow field topology, i.e., the velocity vector

directions and magnitudes, and the streamlines match very well for both measurement techniques. Small deviations were found in the turbulent kinetic energy, i.e., the amount of velocity fluctuations in the flow field. Those deviations might be a result of several reasons. First, they might result from differences in the processing algorithms, since DaVis was used for the HS-TPIV measurements and PIVView was used for the analysis of the HS-SPIV data. Furthermore, small differences in the boundary conditions of the measurements, e.g., temperature or engine speed are a possible explanation. The intake temperature can only be controlled with a limited accuracy and the engine speed might fluctuate slightly depending on oil /engine temperature and the ambient conditions. Most importantly, the flow field inside combustion engines is affected by the cycle-to-cycle variations (CCV). Hence, influences due to CCV are an additional, possible source of the deviations.

4.2 Influence of an Increasing Boost Pressure on the Flow

In the following, the effect of increasing boost pressure on the three-dimensional flow field inside the ICE is discussed. For this analysis, the in-cylinder velocities at several crank angles are investigated. Figures 8 - 10 display the ensemble-averaged velocity vectors in the tumble plane and the isosurfaces of the ensemble-averaged velocity magnitude $U_{mag} = \sqrt{\bar{u}^2 + \bar{v}^2 + \bar{w}^2}$ at 50°, 90°, 180°, 230°, 280°, and 310° atdc.

At 50° atdc (fig. 8 left), the high-velocity flow through the intake valves, which are already halfway open, can be observed. For increasing intake pressure, the velocity vectors of the intake jets are more downwards directed. Furthermore, the area of very high velocity inside the yellow isosurface is larger and expands more into positive x-direction.

A comparable flow field can be found at 90° atdc (fig. 8 right), where velocities above 28 m/s (yellow isosurface) are more common with increasing pressure. While the high velocities are limited to a single area for 1.2 bar and 1.4 bar, two sections of high velocity can be found for 1.0 bar. Furthermore, the velocity magnitude also increases in the bottom left and right part of the measurement volume, which can be seen by the size of the green and blue surfaces. Additionally, the velocity magnitude is not constant in y-direction and decreases towards negative y-direction. Hence, the flow field is not completely symmetrical towards the tumble plane, although the tumble plane is a geometrical symmetry plane of the combustion chamber.

At 180° atdc (fig. 9 left), the intake valves are nearly closed. The flow field is not dominated by the high velocity of the intake jets anymore; it is rather characterized by a well-developed tumble vortex. For an intake pressure of 1.0 bar, one region with high velocity is placed at the right side

of the combustion chamber under the intake valves. Another high-velocity region is placed at the top left and is an effect of the declining intake jets. For increasing boost pressure, the high velocity region towards the right side of the cylinder decreases, but the velocity in the remaining intake jet slightly increases. Furthermore, the velocity near the piston increases significantly, while the low-velocity region around the tumble vortex core is enlarged.

For 1.0 bar at 230° atdc (fig. 9 right), a cylindrical region of increased velocity can be found near the top right of the measurement volume that is reduced for increasing pressure. However, with increasing pressure the velocity in the lower half of the combustion chamber increases.

Figure 10 shows the flow fields during the second half of the compression stroke. At both 280° atdc (left) and 310° atdc (right), a velocity increase is evident in the lower half and in the right side of the cylinder volume for high intake pressures. At the same time, the size of the low-velocity center region of the tumble vortex increases.

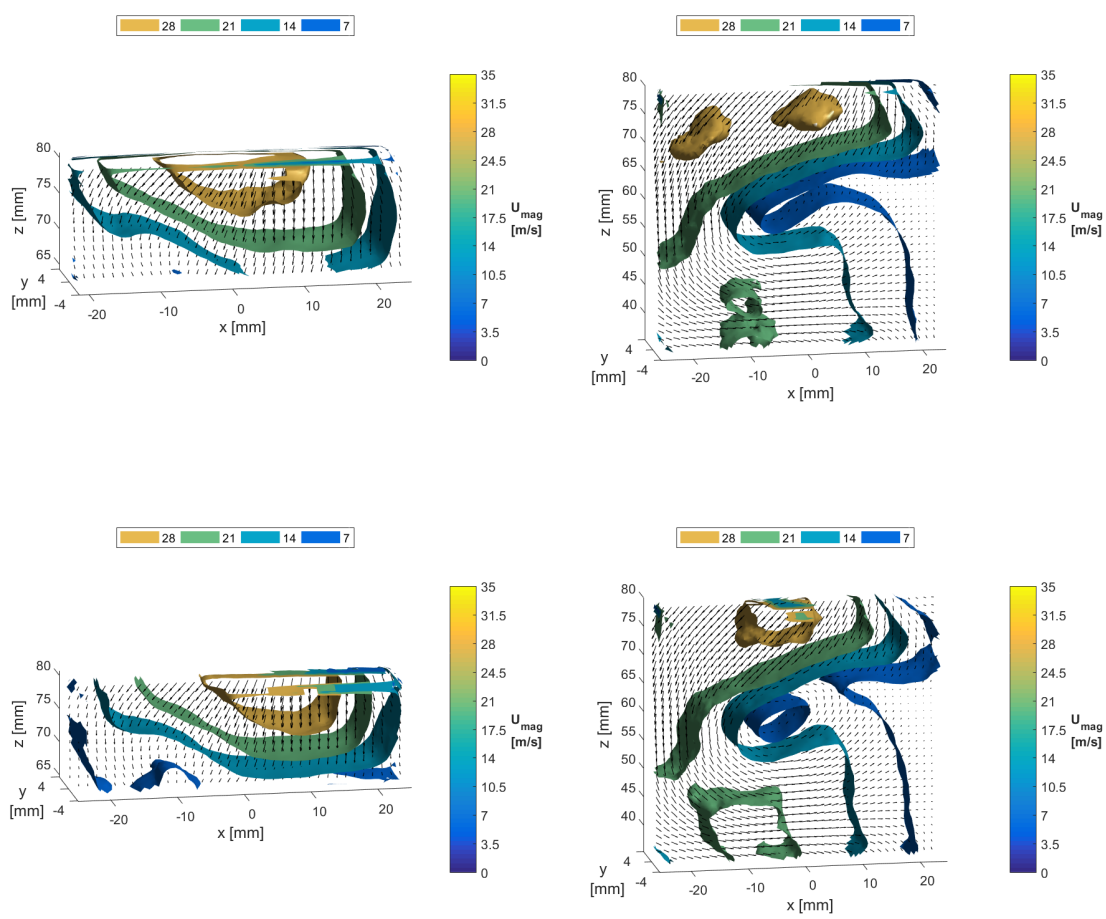

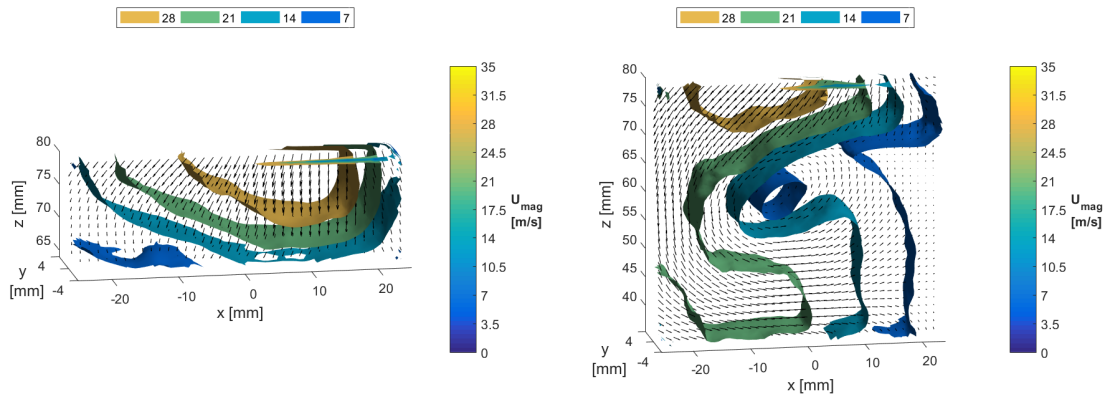

Fig. 8 Ensemble-averaged velocity vectors in the tumble plane and isosurfaces of the ensemble-averaged velocity magnitude U_{mag} for 20 %, 40 %, 60 %, and 80 % of the rounded up maximum of U_{mag} for two different crank angles of 50° atdc (left) and 90° atdc (right) and three different intake pressures of 1.0 bar (top), 1.2 bar (center), and 1.4 bar (bottom).

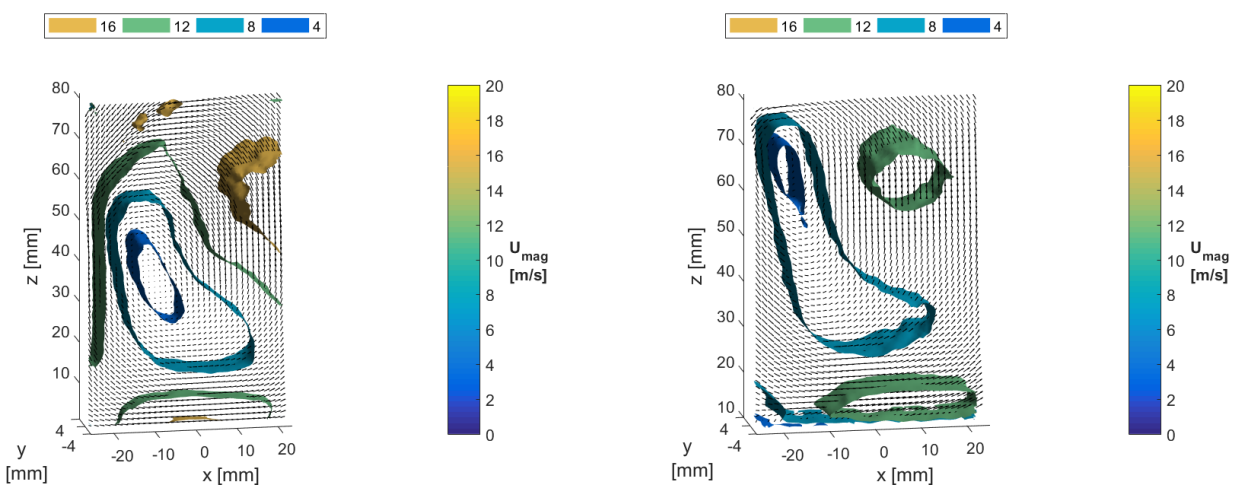

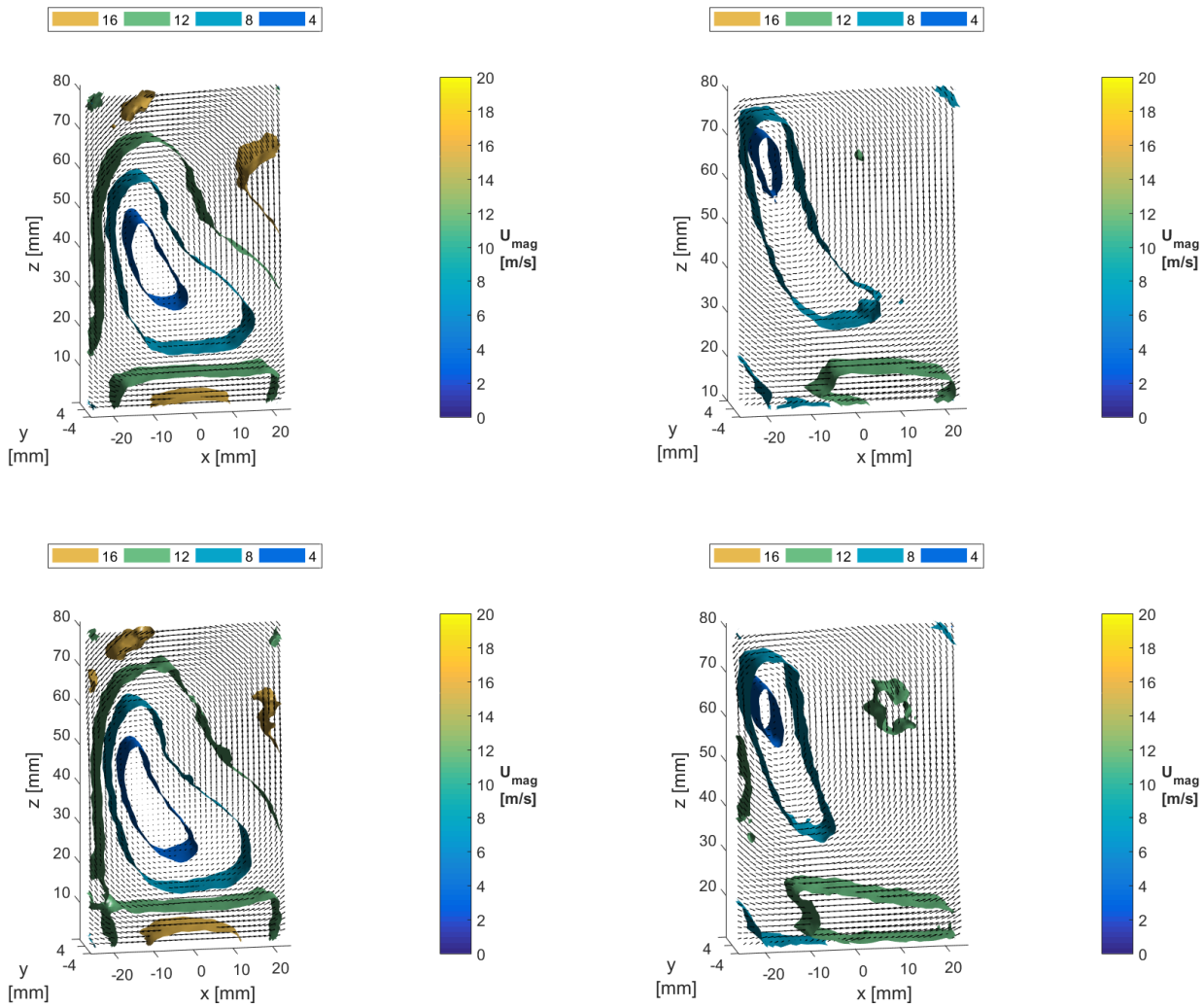

Fig. 9 Ensemble-averaged velocity vectors in the tumble plane and isosurfaces of the ensemble-averaged velocity magnitude U_{mag} for 20 %, 40 %, 60 %, and 80 % of the rounded up maximum of U_{mag} for two different crank angles of 180° atdc (left) and 230° atdc (right) and three different intake pressures of 1.0 bar (top), 1.2 bar (center), and 1.4 bar (bottom).

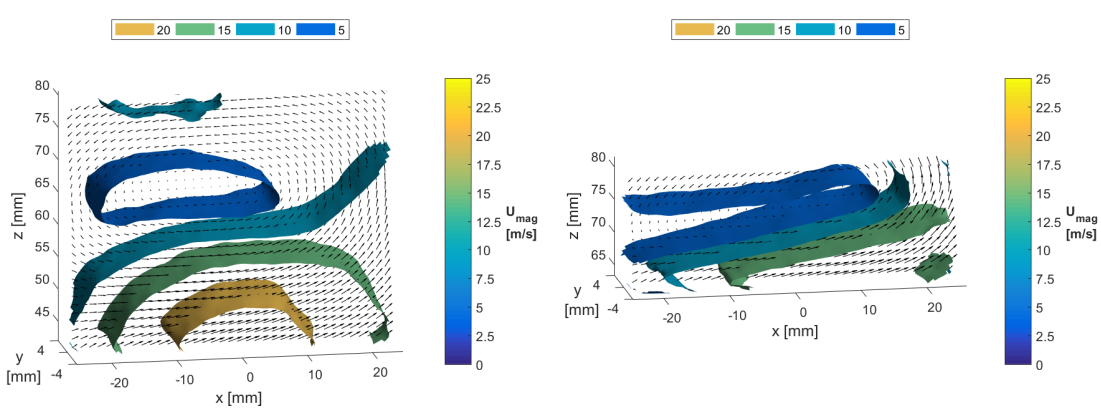

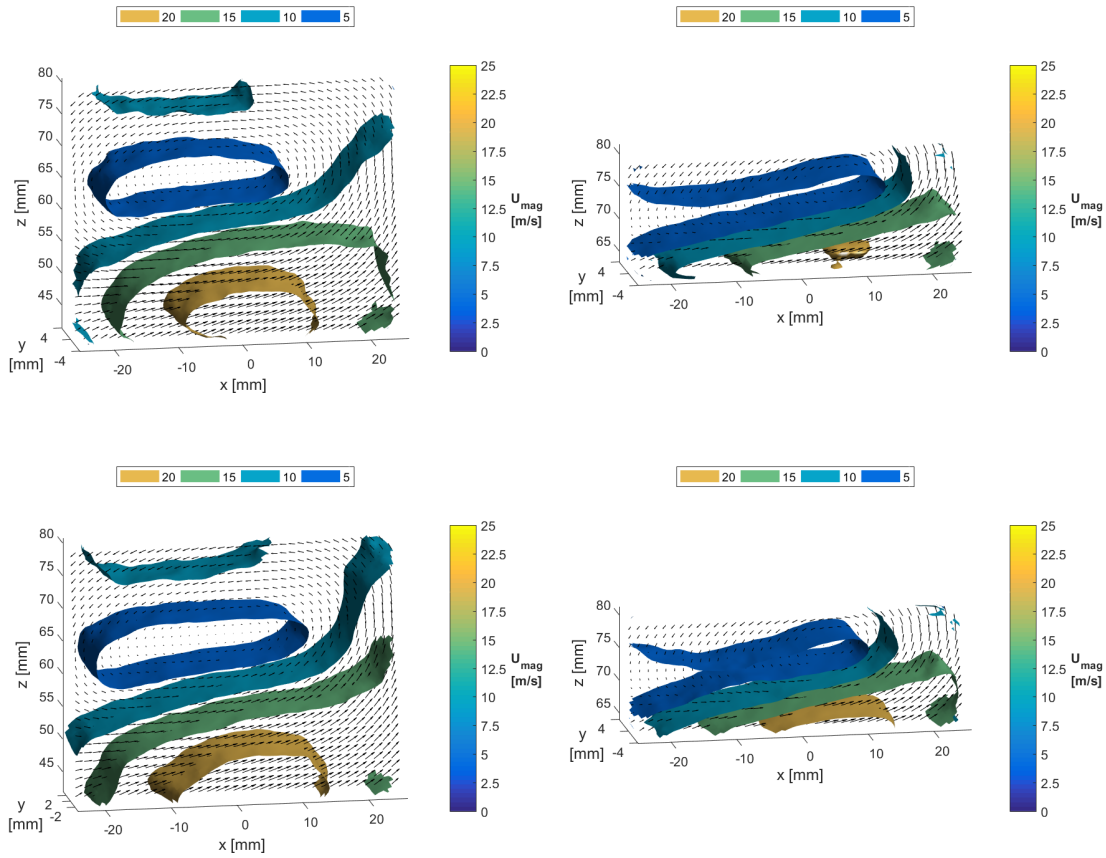

Fig. 10 Ensemble-averaged velocity vectors in the tumble plane and isosurfaces of the ensemble-averaged velocity magnitude U_{mag} for 20 %, 40 %, 60 %, and 80 % of the rounded up maximum of U_{mag} for two different crank angles of 280° atdc (left) and 310° atdc (right) and three different intake pressures of 1.0 bar (top), 1.2 bar (center), and 1.4 bar (bottom).

Figures 8 - 10 clearly show that the general flow topology and the size of the tumble vortex center are affected by the boost pressure. Figure 11 depicts the ensemble-averaged trajectory of the tumble vortex core through the combustion chamber. Evidently, all three trajectories follow more-or-less a similar path and all trajectories start and end at identical locations. However, the core's trajectory is more well-rounded for higher intake pressures.

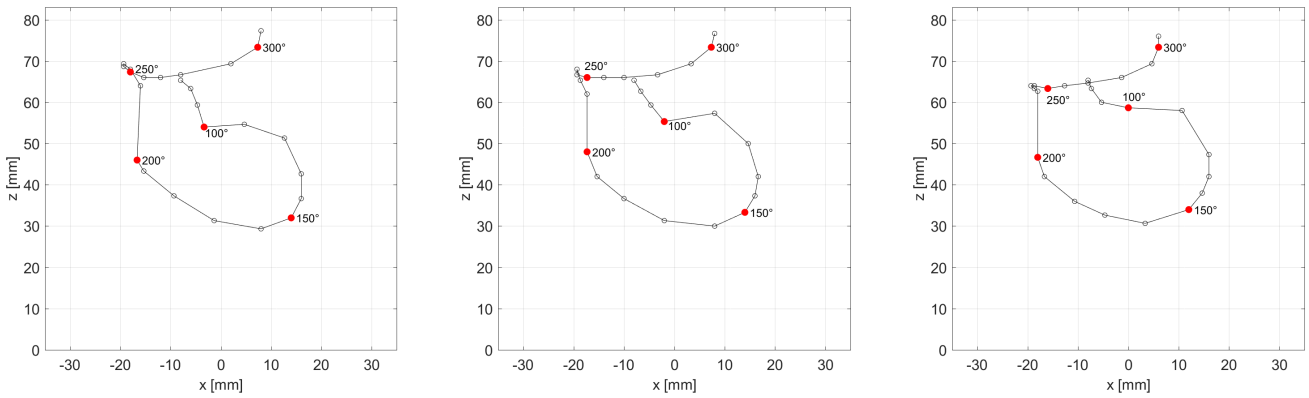

Fig. 11 Ensemble-averaged trajectory of the tumble vortex core in the combustion chamber in the tumble plane (y00) for 1,500 rpm from HS-TPIV. From left to right, the intake pressures 1.0 bar, 1.2 bar, and 1.4 bar are displayed.

The analysis of the flow fields shows that the intake pressure slightly influences the velocity inside the combustion chamber. However, no general velocity increase with increasing boost pressure was found, because at most crank angles the velocity increases locally in some regions while it decreases in other regions. In general, the mean velocity in the combustion chamber remains more-or-less the same. However, due to the increased intake pressure, the charge inside the engine increases, which also increases the density and pressure in the combustion chamber during compression.

5. Conclusion and Outlook

In this work, high-speed tomographic particle-image velocimetry (HS-TPIV) measurements were conducted in an internal combustion engine. To validate the tomographic measurements on the engine test rig, simultaneous high-speed stereoscopic particle-image velocimetry (HS-SPIV) measurements were conducted. The comparison of the experimental findings showed that the results from both measurement techniques are in very good agreement, although there were slight deviations, which were probably an effect of differences in the operating conditions and/or the different processing algorithms of DaVis and PIVView. In combination with the validation, an extensive description of the development of the flow field topology in the symmetry plane was presented.

The results of the HS-TPIV measurements were investigated for three different intake pressures. The investigation of the isosurfaces of the ensemble-averaged velocity magnitude U_{mag} at six different crank angles showed that the intake pressure has an impact on the global flow topology. It was observed that with increasing intake pressure, a slight reallocation of the velocity

distribution inside the cylinder occurs. During the early intake, larger regions of high velocity could be found in the intake jets. At 180° atdc and thereafter, an increasing intake pressure leads to a velocity decrease in the top right region of the combustion chamber, while velocities in the bottom half of the combustion chamber increase. In the second half of the compression stroke, a significant expansion of the low-velocity region around the tumble vortex center could be observed. However, the velocity reduction in this area is compensated by a velocity increase at the bottom of the chamber. Furthermore, it could be observed that the flow field is not exactly symmetrical since the velocities at 90° atdc and 180° atdc decrease in negative y-direction. Additionally, the investigation of the ensemble-averaged trajectory of the core of the tumble vortex core showed a more-rounded path of the vortex through the combustion chamber.

The measurements of this study showed that the HS-TPIV test setup yields valid measurement results that allow a more insightful investigation of the flow field in internal combustion engines. Furthermore, first volumetric measurements of the impact on boost pressure on the flow field of the investigated ICE were presented and discussed in detail. In future works, the test setup will be adjusted to yield higher temporal or spatial resolution. The higher spatial resolution will enable a better investigation of the 3D character of the flow field because of the increased depth of the measurement volume. However, an increase in temporal or spatial resolution demands higher light intensities due to the increased focal number, the increased size of the measurement volume, and the reduction of laser energy with increasing frame rate. Therefore, different seeding techniques have to be applied. Furthermore, future work will feature the investigation of instantaneous flow fields to analyze CCV.

References

- Baum E, Peterson B, Surmann C, Michaelis D et al. (2012) Investigation of the 3D flow field in an IC engine using tomographic PIV. Proceddings of the Combustion Institute 34(2):2903-2910. doi:10.1016/j.proci.2012.06.123
- Baumgarten C (2006) Mixture Formation in Internal Combustion Engines. Springer, Friedrichshafen. ISBN: 978-354-03-0836-2. doi:10.1007/3-540-30836-9
- Benedict L, Gould R (1996) Towards better uncertainty estimates for turbulence statistics. Experiments in Fluids 22:129-136. doi:10.1007/s003480050030
- Brassat A, Thewes M, Müther M, Pischinger S (2011) Massgeschneiderte Kraftstoffe aus Biomasse für Ottomotoren. MTZ Motortechnische Zeitschrift 72(12):988–995. doi:10.1365/s35146-011-0212-2

- Braun M, Palmer J, van Overbrüggen T, Klaas M et al. (2017) Influence of In-Cylinder Air Flow on Spray Propagation. SAE International Journal of Engines 10(4):1398–1410. doi:10.4271/2017-01-9280
- Braun M, Klaas M, Schröder W (2018) Influence of Miller Cycles on Engine Air Flow. SAE International Journal of Engines 11(2):2018. doi:10.4271/03-11-02-0011.
- Bücker I, Karhoff DC, Klaas M, Schröder W (2012) Stereoscopic multi-planar PIV measurements of in-cylinder tumbling flow. Experiments in Fluids 53(6):1993–2009. doi:10.1007/s00348-012-1402-5
- Bücker I, Karhoff DC, Klaas M, Schröder W (2013) Engine In-Cylinder Flow Control via Variable Intake Valve Timing. SAE Technical Paper 2013-24-0055. doi:10.4271/2013-24-0055
- Daniel R, Tian G, Xu H, Wystynski ML et al. (2011) Effect of spark timing and load on a DISI engine fuelled with 2,5-dimethylfuran. Fuel 90(2):449–458. doi:10.1016/j.fuel.2010.10.008
- Dannemann J, Pielhop K, Klaas M, Schröder W (2011) Cycle Resolved Multi-Planar Flow Measurements in a Four-Valve Combustion Engine. Experiments in Fluids 50(4):961-976. doi:10.1007/s00348-010-0963-4
- Druault P, Guibert P, Alizon F (2005) Use of proper orthogonal decomposition for time interpolation from PIV data. Experiments in Fluids 39(6):1009–1023. doi:10.1007/s00348-005-0035-3
- Gadekar S, Singh A, Agarwal A (2016) Tomographic PIV Evaluation of In-Cylinder Flow Evolution and Effect of Engine Speed. SAE Technical Paper 2016-01-0638. doi:10.4271/2016-01-0638
- Graftieaux L, Michard M, Grosjean N (2001) Combining PIV, POD and Vortex Identification Algorithms for the Study of Unsteady Turbulent Swirling Flows. Measurement Science and Technology 12(9):1422. doi:10.1088/0957-0233/12/9/307
- Heywood JB (1988) Internal combustion engine fundamentals. McGraw-Hill, New York. ISBN: 0-07-028637-X
- Hoppe F, Burke U, Thewes M, Heufer A et al. (2016) Tailor-Made Fuels from Biomass: Potentials of 2-butanone and 2-methylfuran in direct injection spark ignition engines. Fuel 167:106–117. doi:10.1016/j.fuel.2015.11.039
- Janssen A, Müther M, Pischinger S, Kolbeck A et al. (2009) Tailor-Made Fuels: The Potential of Oxygen Content in Fuels for Advanced Diesel Combustion Systems. SAE Technical Paper 2009-01-2765. doi:10.4271/2009-01-2765
- Lumley JL (1967) The structure of inhomogenous turbulent flows. Atmospheric Turbulence and Radio Wave Propagation, Nauka, Moskau, 166 – 178.

- Lumley JL (1999) Engines. An Introduction. Cambridge University Press, Cambridge. ISBN: 0-521-64277-9
- Shafiee S, Topal E (2009) When will fossil fuel reserves be diminished? Energy policy 37(1):181-189. doi:10.1016/j.enpol.2008.08.016
- Singh A, Gupta A, Agarwal A (2015) Tomographic Particle Image Velocimetry for Flow Analysis in a Single Cylinder Optical Engine. SAE International Journal of Materials and Manufacturing 8(2). doi:10.4271/2015-01-0599
- Singh BR, Singh O (2012) Global Trends of Fossil Fuel Reserves and Climate Change in the 21st Century. In: Khan S (ed) Fossil Fuel and the Environment, In Tech, 168-192. ISBN: 978-953-51-0277-9
- Thewes M, Müther M, Pischinger S, Budde M et al. (2011) Analysis of the Impact of 2-Methylfuran on Mixture Formation and Combustion in a Direct-Injection Spark-Ignition Engine. Energy & Fuels 25(12):5549–5561. doi:10.1021/ef201021a
- Van Overbrüggen T, Klaas M, Bahl B, Schröder W (2015) Tomographic Particle-Image Velocimetry Analysis of In-Cylinder Flows. SAE International Journal of Engines 8(3). doi:10.4271/2015-01-9042

Acknowledgements

This work was performed as part of the Cluster of Excellence “Tailor-Made Fuels from Biomass”, which is funded by the Excellence Initiative of the German federal and state governments to promote science and research at German universities. Furthermore, this research is part of the project "Analysis of cycle-to-cycle variations in IC engines using highspeed Tomographic Particle-Image Velocimetry" funded by the German Research Association (Deutsche Forschungsgemeinschaft, DFG).